Full length article

Irradiation damage in $(Zr_{0.25}Ta_{0.25}Nb_{0.25}Ti_{0.25})C$ high-entropy carbide ceramics

Fei Wang[a], Xueliang Yan[a], Tianyao Wang[b], Yaqiao Wu[c,d], Lin Shao[b], Michael Nastasi[b], Yongfeng Lu[e], Bai Cui[a,f,*]

[a] Department of Mechanical & Materials Engineering, University of Nebraska–Lincoln, Lincoln, NE 68588, United States
[b] Department of Nuclear Engineering, Texas A&M University, TX 77843, United States
[c] Micron School of Materials Science and Engineering, Boise State University, Boise, ID 83725, United States
[d] Center for Advanced Energy Studies, Idaho Falls, ID 83401, United States
[e] Department of Electrical Engineering, University of Nebraska-Lincoln, 1400 R St, Lincoln, NE 68588, United States
[f] Nebraska Center for Materials and Nanoscience, University of Nebraska–Lincoln, Lincoln, NE, 68588, United States

ARTICLE INFO

ABSTRACT

This research revealed the mechanisms of irradiation damage in the novel high entropy ceramic materials. $(Zr_{0.25}Ta_{0.25}Nb_{0.25}Ti_{0.25})C$ high-entropy carbide ceramics (HECC) with a single-phase rock-salt structure was synthesized by spark plasma sintering, which was irradiated by 3 MeV Zr ions to 20 dpa at 25, 300, and 500 °C. X-ray diffraction analysis showed that $(Zr_{0.25}Ta_{0.25}Nb_{0.25}Ti_{0.25})C$ maintained a high phase stability without phase transformation after irradiation. About 0.2% lattice parameter expansion was revealed. The irradiation-induced microstructures were comprised of defect clusters with diameters of several nanometers, without void formation or radiation-induced segregation. The defect clusters were characterized by transmission electron microscopy as two types of dislocation loops, including perfect loops with Burgers vectors of $\boldsymbol{b} = a/2<1\ 1\ 0>$ and faulted Frank loops with Burgers vectors of $\boldsymbol{b} = a/3<1\ 1\ 1>$. The growth of dislocation loops may be suppressed by the strong local lattice distortion. Nanoindentation tests showed irradiation-induced hardness increase, which was possibly caused by dislocation loops and lattice strain. Overall, the high irradiation resistance, along with other excellent physical properties makes HECC promising structural materials for advanced reactor designs.

1. Introduction

Key structural components in the Generation-IV fission reactors and the future fusion reactors require new materials to fulfill the needs under extreme conditions, such as high temperatures (>700 °C), high stress, high neutron damage, and high transmutation gas sustainability [1,2]. In order to serve in these extreme environments, novel materials must demonstrate outstanding resistance to neutron irradiation damage, corrosive coolants, thermal and irradiation creep, helium embrittlement, and so on.

The idea of entropy stabilization has created promising opportunities for new material design and discovery. High entropy alloys (HEAs) have gained great attentions in recent years [3,4]. Unlike traditional metal alloys, HEAs contain more than four metal elements in equal or near-equal concentrations but can form a stable single-phase lattice structure [5]. The compositional complexity in HEAs results in a high configurational entropy that may improve the phase stability [6]. The extensive studies on HEAs revealed that they are potential candidates for nuclear applications due to their superior mechanical properties [7,8], corrosion resistance [9,10], and irradiation tolerance [11,12]. In HEAs such as NiCoFeCr [13] and $Ti_2ZrHfV_{0.5}Mo_{0.2}$ [14], it is suggested that an increasing number of principal elements and/or concentrations of specific elements can result in a substantial reduction in the electron mean free path and a decrease in electrical and thermal conductivity [15,16]. The subsequently slow energy dissipation can affect the defect dynamics at early stages, which may suppress the formation of irradiation defect clusters.

Compared to the extensively studied HEAs, high entropy ceramics (HECs) are recently discovered and less investigated. HECs include oxides [17,18], borides [19,20], and carbides [21,22]. They are characterized by multiple metal elements in an equal atomic ratio in the cation position, while a nonmetal element (O, B, or C) occupies the anion position. Among them, high-entropy carbide

---

ceramics (HECCs) have shown some unique physical properties that result from the entropy stabilization such as significant lattice distortion. These unique physical properties include lower thermal conductivity [22], higher nanohardness (>40 GPa) [23–25], and an improved oxidation resistance [26–28] than the binary transition metal carbides such as ZrC. In addition, HECCs are presumed to inherit other physical properties of binary carbides, such as high melting temperature and corrosion resistance. Because of these excellent properties, HECCs may be promising structural materials for Generation-IV nuclear systems such as the gas-cooled fast reactor (GFR) and the very-high-temperature reactor (VHTR).

Earlier, our team first reported a preliminary study on $(Hf_{0.2}Zr_{0.2}Ta_{0.2}Nb_{0.2}Ti0_{0.2})C$ after 120 keV helium ion irradiation at 25 °C, which showed that the coalescence of helium bubbles was significantly suppressed [29]. $(Zr_{0.25}Ta_{0.25}Nb_{0.25}Ti_{0.25})C$ was later developed in which the Hf element was removed from the composition due to its high neutron absorption cross-section. It is hypothesized that HECCs such as $(Zr_{0.25}Ta_{0.25}Nb_{0.25}Ti_{0.25})C$ have similar mechanisms with HEAs for recovery from radiation damage, and thus present a high irradiation tolerance. The potential mechanisms may be related to the impact of compositional complexity on the energy dissipation [16,30], damage accumulation [31], and kinetics of defect mobility and migration [32,33] in materials.

The feasibility of HECCs in nuclear applications is also motivated by the binary transition metal carbide ZrC [34]. ZrC is a candidate material for the carbide-based composite-type fuels in GFR [35] as well as the coating material for TRISO particle fuels in the high-temperature gas-cooled reactor (HTGR) [36]. There is extensive literature on the irradiation defects in ZrC. Yang et al. investigated the irradiation response in stoichiometric ZrC with a 2.6 MeV proton irradiation at 800 °C at 0.7 and 1.5 dpa [37]. The irradiation-induced microstructures mainly consisted of a high density of faulted Frank loops, while no irradiation-induced amorphization, voids, or precipitates were observed. Ulmer et al. studied the microstructural evolution in $ZrC_{0.8}$ and $ZrC_{0.9}$ under in situ irradiation experiments in the Intermediate Voltage Electron Microscope (IVEM) using 1 MeV Kr^{2+} ions up to 12.8 dpa at −253 to 800 °C [38]. In the low temperature regime (<300 K), the irradiation damage was observed in the form of small defect clusters or "black dots." In the high temperature regime (>873 K), the visible defects did not migrate but interacted with the neighboring defects resulting in coarsening of the defect clusters. It is noted that structural swelling (i.e., lattice parameter expansion) is a common feature that occurred after neutron, proton, and ion irradiation of ZrC ceramics [36,39,40].

The aim of this manuscript is to reveal the mechanisms of irradiation damage in the novel high entropy ceramic materials, using $(Zr_{0.25}Ta_{0.25}Nb_{0.25}Ti_{0.25})C$ as a model material of HECC. Single-phase $(Zr_{0.25}Ta_{0.25}Nb_{0.25}Ti_{0.25})C$ sample was synthesized by spark plasma sintering (SPS). The microstructural stability and evolution under heavy ion irradiation at room and elevated temperatures were investigated using transmission electron microscopy (TEM). The phase stability, formation of irradiation-induced defect clusters, radiation-induced segregation, and irradiation hardening behaviors were carefully studied to provide fundamental mechanisms governing the irradiation damage in $(Zr_{0.25}Ta_{0.25}Nb_{0.25}Ti_{0.25})C$.

2. Experimental procedures

$(Zr_{0.25}Ta_{0.25}Nb_{0.25}Ti_{0.25})C$ samples were fabricated by the SPS process. Commercial powders of ZrC (99.5%, <45 μm), TaC (99.5%, <45 μm), NbC (99.0%, <45 μm), and TiC (99.5%, <45 μm) from Alfa Aesar were used for the synthesis. The powders were mixed at an equimolar ratio (ZrC: TaC: NbC: TiC =1: 1: 1: 1) in Ar atmosphere. The powder mixture was ball milled (Model Pulverisette 7, Fritsch

Gmbh) with 10 mm diameter stainless steel balls (ball-to-powder ratio: 5:1) at 250 rpm for 6 h. To avoid overheating of the powders, the ball milling process was paused for 5 min after every 15 min of milling. SPS of the ball-milled powders was conducted on an SPS system (Model 10-4, Thermal Technologies) under a low vacuum of 2×10^{-2} Torr. The SPS conditions were 2000 °C for 5 min at a pressure of 30 MPa. The as-synthesized samples were discs with 20 mm in diameter and 3 mm in thickness. The as-synthesized samples were grinded to 1 mm thickness and then polished by using 15, 9, 6, 3, and 1 μm diamond lapping films to a mirror finish.

The heavy ion irradiation experiments of $(Zr_{0.25}Ta_{0.25}Nb_{0.25}Ti_{0.25})C$ samples were conducted in the Ion Beam Laboratory at Texas A&M University. The samples were irradiated by 3 MeV zirconium ions (Zr^{2+}) to a maximum fluence of 8.0×10^{15} ions/cm^2 (equivalent to 20 peak dpa) with a dose rate of 1.5×10^{11} ions/cm^2/s at 25, 300, and 500 °C, respectively. The implantation range of 3 MeV Zr^{2+} was 1500 nm. Displacements per atom (dpa) and range were calculated by the Stopping and Range of Ions in Matter (SRIM) simulation code using the full-cascade model following the recent recommendations by Weber et al. [41]. A challenge for the SRIM simulation is overestimation of electronic stopping power in compound targets containing light elements (e.g., C in carbides). Based on the recent evaluation and discussions by Weber et al. [41], the full cascade TRIM simulations is validated and recommended for use in multi-elemental targets such as carbides. The displacement energies of the elements were taken as the default values in the SRIM software as 24 eV for Ti, Ta, Nb, Zr, and 25 eV for C.

Grazing incidence X-ray diffraction (GIXRD) measurements were performed to analyze the structure modification in the near-surface irradiated region of $(Zr_{0.25}Ta_{0.25}Nb_{0.25}Ti_{0.25})C$ samples. A Cu X-ray tube with operation conditions of 40 kV and 44 mA was used in the X-ray diffractometer (SmartLab, Rigaku). The incident beam was fixed at 2° relative to the sample surface. Diffraction patterns were acquired over the 2θ range of 30–90° with a step size 0.02° and dwell time of 1 s at each step. The lattice parameter was refined by Rietveld analysis with the Match and FullProf software [42]. Scanning electron microscopy (SEM) of microstructures was conducted on a FIB/SEM dual-beam workstation (Helios 660 NanoLab, FEI) using secondary electron imaging mode. Energy-dispersive X-ray spectroscopy (EDS) was conducted by an EDS detector (Octane Super, EDAX) to reveal the element distribution. Transmission electron microscopy (TEM) specimens were extracted perpendicular to the sample surface using a standard lift-out technique on FEI Helios 660. To minimize the ion beam damage, the FIB milling process was conducted as follows: TEM lamellae were lifted out and thinned to ~100 nm thickness using 30, 16, 8, and 5 keV Ga ion beam sequentially, followed by cleaning with 2 keV Ga ion beam. TEM characterization of irradiation defects and irradiation-induced phase transformations in irradiated $(Zr_{0.25}Ta_{0.25}Nb_{0.25}Ti_{0.25})C$ samples were carried out on an S/TEM system (Tecnai Osiris, FEI) operated at 200 kV. The diameter and volumetric density of dislocation loops were measured from TEM images. At least 200 loops were measured on each sample to obtain the average diameter. The volumetric density of dislocation loops was calculated as the number of dislocation loops in a unit volume of the TEM foil. The foil thickness was measured from SEM images by rotating the foil surface parallel to the electron beam. The Burgers vector of dislocation loops was identified by the classic $\boldsymbol{g \cdot b}$ analysis [43]. Radiation-induced segregation (RIS) was analyzed on another scanning transmission electron microscopy (STEM) system (Tecnai TF30-FEG STwin, FEI) operated at 300 kV. EDS element distribution was performed using a SiLi EDS detector (EDAMIV/DPP II, EDAX). An electron-beam probe of 1.0 nm diameter was obtained in this instrument for EDS chemical analysis.
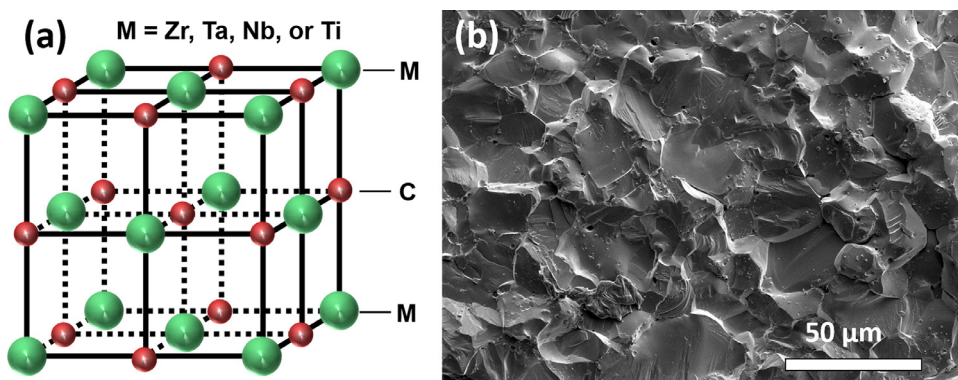
Fig. 1. (a) Schematic diagram of the rock-salt structure of $(Zr_{0.25}Ta_{0.25}Nb_{0.25}Ti_{0.25})C$ high-entropy carbide ceramic (HECC). (b) SEM image of the fracture surface.

Nanoindentation test of the $(Zr_{0.25}Ta_{0.25}Nb_{0.25}Ti_{0.25})C$ samples before and after irradiation was conducted on a triboindenter (Hysitron TI950, Bruker) with a Berkovich tip using various loads from 1000 μN to 12,000 μN, corresponding to a displacement of about 30–150 nm. The loading and unloading time were 10 s and the dwell time was 5 s in each indentation test. The displacements were chosen based on the SRIM simulation to avoid the influence of the unirradiated region beyond the irradiated zone. The spacing between indentations was at least 20 μm to avoid the effect of strain fields. The measured hardness decreased with the indentation depth due to the indentation size effect [44]. Thus, the Nix and Gao method [45] was used to determine the hardness of both unirradiated and irradiated samples. The depth dependence of hardness can be described as:

$$\frac{H}{H_0} = \sqrt{1 + \frac{h^*}{h}} \tag{1}$$

where H is the hardness at the indentation depth of h; H_0 is the hardness at infinite depth (i.e., real hardness of the material that eliminates the indentation size effect); and h^* is a characteristic length that depends on the shape of the indenter, the shear modulus and H_0. Based on Eq. (1), there is a linear relationship between H^2 and $1/h$. The real hardness H_0 can be extrapolated from the measured harnesses in different depths.

3. Results and discussions

XRD pattern of the as-synthesized $(Zr_{0.25}Ta_{0.25}Nb_{0.25}Ti_{0.25})C$ can be indexed as a single-phase rock-salt structure with space group Fm$\bar{3}$m (see Fig. 3), which is consistent with other high-entropy carbide ceramics with similar element compositions [22,39]. In the rock-salt structure of $(Zr_{0.25}Ta_{0.25}Nb_{0.25}Ti_{0.25})C$, the metal elements (Zr, Ta, Nb, and Ti) very likely share the cation sublattice with a face-centered cubic (FCC) structure, while the C element is in the anion FCC sublattice (Fig. 1a). The lattice parameter a of $(Zr_{0.25}Ta_{0.25}Nb_{0.25}Ti_{0.25})C$ was calculated to be 4.489 Å. The theoretical density was calculated from its lattice parameter to be 8.46 g/cm^3. The measured density of the bulk $(Zr_{0.25}Ta_{0.25}Nb_{0.25}Ti_{0.25})C$ sample using the Archimedes method was 8.25 g/cm^3, suggesting a relative density of 97.5%. SEM analysis of a typical fracture surface of the $(Zr_{0.25}Ta_{0.25}Nb_{0.25}Ti_{0.25})C$ sample revealed uniaxial grains with an average grain size of 19 μm (Fig. 1b). EDS mapping analysis of Zr, Ta, Nb and Ti elements showed these metal cation elements are homogeneously distributed at the micrometer level.
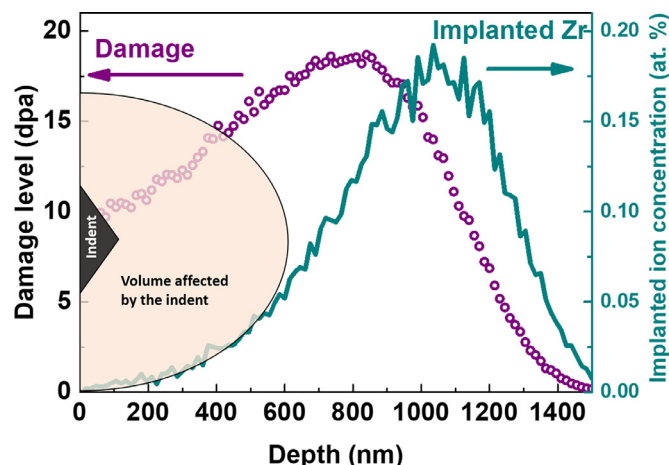

Fig. 2. SRIM calculation of the displacement damage (dotted purple line) and Zr ion implantation (solid green line) profiles by 3 MeV Zr^{2+} irradiation in $(Zr_{0.25}Ta_{0.25}Nb_{0.25}Ti_{0.25})C$ at a fluence of 8.0 $\times$ 10^{15} ions/cm^2. Overlaid with schematic diagram of nanoindentation with plastic zone. The nanoindentation direction is performed parallel to the incident ion beam direction.

3.1. SRIM calculation of irradiation damage

Fig. 2 shows the depth profiles of displacement damage and implanted atoms by 3 MeV Zr^{2+} irradiation calculated using the SRIM simulation. At the maximum fluence of 8.0 $\times$ 10^{15} ions/cm^2, the peak displacement damage is about 20 dpa in $(Zr_{0.25}Ta_{0.25}Nb_{0.25}Ti_{0.25})C$ at a depth of about 830 nm.

3.2. XRD characterization

GIXRD characterizations were performed on the $(Zr_{0.25}Ta_{0.25}Nb_{0.25}Ti_{0.25})C$ HECC samples after irradiation to characterize the potential irradiation-induced phase transformations (Fig. 3a). There was no significant change in GIXRD peaks in the irradiated samples, suggesting that no phase transformation occurred in $(Zr_{0.25}Ta_{0.25}Nb_{0.25}Ti_{0.25})C$ after Zr^{2+} irradiation to 20 dpa at 25 and 500 °C, respectively. The main changes in the GIXRD patterns are slight peak shift and broadening. There is a small peak shift to lower 2θ values after irradiation (Fig. 3b). The lattice parameters were refined by Rietveld analysis, suggesting a lattice parameter increase of 0.22% after irradiation to 20 dpa at 25 °C and 0.19% at 500 °C, respectively (Fig. 3c). The peak broadening may be attributed to the formation of irradiation defects [46].

Lattice expansion has been generally observed after heavy ion, proton, and neutron irradiation of ZrC at dose levels above 0.2
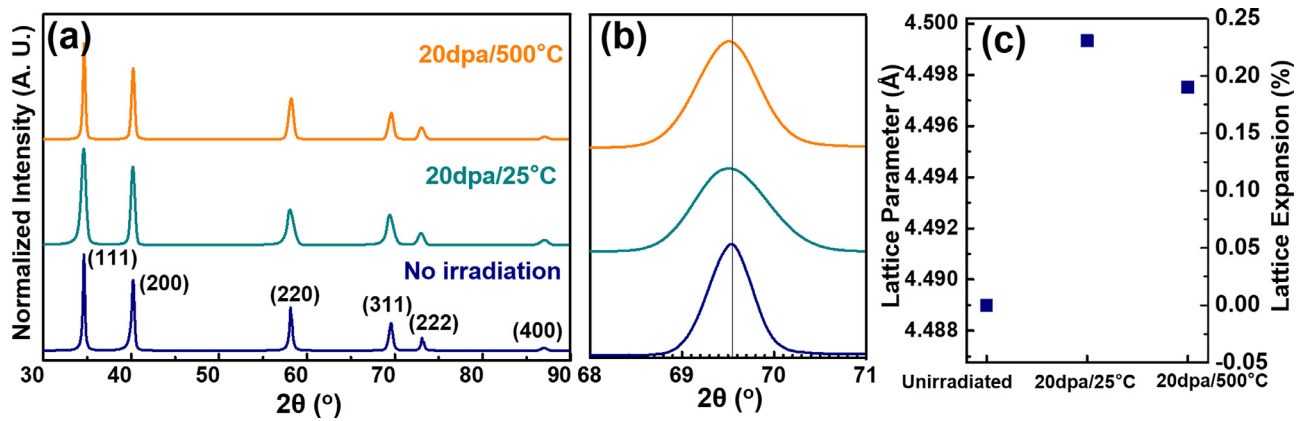
Fig. 3. (a) Comparison of GIXRD patterns of $(Zr_{0.25}Ta_{0.25}Nb_{0.25}Ti_{0.25})C$ before and after 3 MeV Zr ion irradiation to 20 dpa at 25 and 500 °C, respectively; (b) the enlarged view of the (2 2 2) diffraction peak shift; (c) the calculated lattice parameters and increments after irradiation.

dpa [37,47,48]. Pellegrino et al. [49] reported lattice expansion in single crystal ZrC was 0.23% after 1.2 MeV Au^+ irradiation at room temperature. Florez et al. found that during 10 MeV Au^{3+} ion irradiation at 800 °C, the lattice parameter of ZrC had an initial rapid increase at low dose, followed by collapse to a lower level of lattice expansion when the formation of dislocation loops became significant [46]. The lattice expansion of 0.13% was reported for ZrC irradiated by 4 MeV Au ion to 7 dpa at 25 °C [34]. For 1 MeV Kr ion irradiated ZrC, the lattice expansion was 0.7% and 0.9% after irradiation to 10 dpa and 30 dpa at 27 °C, respectively [50]. Yang et al. reported that the lattice expansions are 0.09% and 0.11% at 0.7 and 1.5 dpa, respectively, after irradiation of ZrC to 2.6 MeV proton at 800 °C [51]. A lattice expansion of 0.2–0.8% was reported after neutron irradiation of ZrC to 3 dpa at 300–700 °C [48]. Keilholtz et al. found the lattice expansions in TiC, ZrC, TaC, and NbC were 0.6 to 1% after fast neutron irradiation at 300 to 700 °C at a neutron dose of $1\sim2 \times 10^{21}$ cm^{-2} [48]. Agarwal et al. [52] reported that lattice expansion in TiC decreased with temperature, from 0.7% at 200 °C to 0.4% at 620 °C, following neutron irradiation to 2 dpa. Thus, the literature suggests that in general the lattice expansion in Zr^{2+}-irradiated $(Zr_{0.25}Ta_{0.25}Nb_{0.25}Ti_{0.25})C$ is in the similar range with that in ion- and neutron-irradiated ZrC. However, the direct comparison of lattice expansion between $(Zr_{0.25}Ta_{0.25}Nb_{0.25}Ti_{0.25})C$ and ZrC under the same irradiation conditions will be necessary in the future studies.

3.3. Evolution of irradiation-induced defect clusters

Fig. 4 shows the weak-beam dark-field (WBDF) TEM images of the cross-sectional microstructures in $(Zr_{0.25}Ta_{0.25}Nb_{0.25}Ti_{0.25})C$ samples before and after 3 MeV Zr ion irradiation to 20 dpa at 25, 300, and 500 °C. TEM images were taken near [0 1 1] zone axis under the WBDF condition using diffraction vector **g**=(0 2 −2). In the TEM images of the $(Zr_{0.25}Ta_{0.25}Nb_{0.25}Ti_{0.25})C$ sample before irradiation (Fig. 4a), the white dots indicated very small defect clusters with an average diameter of 0.7 nm, which were induced by the Ga ion beam damage during the FIB ion milling process. The size of the FIB damage was much smaller than defect clusters created by 3 MeV Zr ions (Fig. 4b–d) that had an average diameter of 2.5 nm. The larger bright dots in the TEM images of the irradiated samples are irradiation-induced defect clusters, which appear as dislocation loops according to their morphology. The Burgers vectors, size, number density, and distribution of these irradiation-induced defect clusters were carefully characterized and presented below.

The Burgers vectors of the defect clusters were first identified by the classic **g·b** analysis [43]. After irradiation to 20 dpa at 25 and 300 °C, defect clusters are too small (< 3 nm) with a high number density, which makes the **g·b** analysis difficult. The feasible **g·b** analysis was performed in the $(Zr_{0.25}Ta_{0.25}Nb_{0.25}Ti_{0.25})C$ sample after irradiation to 20 dpa at 500 °C in which the size of the defect cluster is larger than 3 nm.

Table 1 lists the possible Burgers vectors (**b**) of dislocation loops, **g** vectors and **g·b** results. Fig. 5 shows the bright-field TEM images of the dislocation loops at same location using different **g** vectors of <3 −1 1>, <2 0 0>, <0 2 0>, and <2 −2 0> by tilting the sample to the [0 1 1] and [0 0 1] zone axis, respectively. The Burgers vector of dislocation loops were identified by comparing the four images in Fig. 5 and applying the visibility criteria. The loops with the same Burgers vector were marked by circles in the same color. For example, the dark red circles mark the dislocation loops with b=±a/2[0 1 1] that are invisible under **g** = [3 −1 1] (Fig. 5a) and **g** = [2 0 0] (Fig. 5b), but become visible under **g** = [0 2 0] (Fig. 5c) and **g** = [2 −2 0] (Fig. 5d). The orange, blue, purple, and black circles denote the dislocation loops with b=±a/2[1 0 1] or =±a/2[−1 0 1], b=±a/2[0 −1 1], b=±a/2[1 1 0] or a/3 [1 1 1] or a/3 [1 1 −1], and b=±a/2[1 −1 0] or ±a/3[1 −1 1] or ±a/3[−1 1 1]. Thus, the Burgers vectors of most dislocation loops in the color circles are in the family of **b** = a/2<1 1 0>.

$(Zr_{0.25}Ta_{0.25}Nb_{0.25}Ti_{0.25})C$ has a rock-salt structure in which the metal cations occupy an FCC sublattice. In FCC metals such as Ni or austenitic steels, the irradiation-induced defect clusters with the Burgers vectors of **b** = a/2<1 1 0> are perfect dislocation loops, while those with Burgers vector of **b** = a/3<1 1 1> are faulted dislocation loops (i.e., Frank loops) [53,54]. Therefore, most dislocation loops in the color circles in Fig. 5 are presumed to be perfect dislocation loops formed in the cation sublattice in $(Zr_{0.25}Ta_{0.25}Nb_{0.25}Ti_{0.25})C$ by the heavy ion irradiation.

Rel-rod imaging technique was then used to verify and characterize the Frank loops in $(Zr_{0.25}Ta_{0.25}Nb_{0.25}Ti_{0.25})C$ sample after irradiation to 20 dpa at 500 °C [55]. Fig. 6a and b show the rel-rod dark-field TEM images of the Frank loops on (1 1 1̄) and (1 1̄ 1) planes, respectively. These results confirm the formation of faulted Frank loops with the Burgers vector of **b** = a/3<1 1 1> in $(Zr_{0.25}Ta_{0.25}Nb_{0.25}Ti_{0.25})C$, which is presumed to form in the cation sublattice of metal elements by the heavy ion irradiation.

Fig. 7 shows the diameter and volumetric density of dislocation loops in the $(Zr_{0.25}Ta_{0.25}Nb_{0.25}Ti_{0.25})C$ samples after irradiation to 20 dpa as a function of temperature and depth, which were measured from weak-beam dark-field TEM images (including Fig. 4 and other TEM images at higher magnification). Along the depth, the diameter of dislocation loops is almost the same, and slightly increases with the irradiation temperature from 1.6 nm at 25 °C to 2.3 nm at 500 °C (Fig. 7a). The number density of dislocation loops has a larger variation with the depth; the peak is
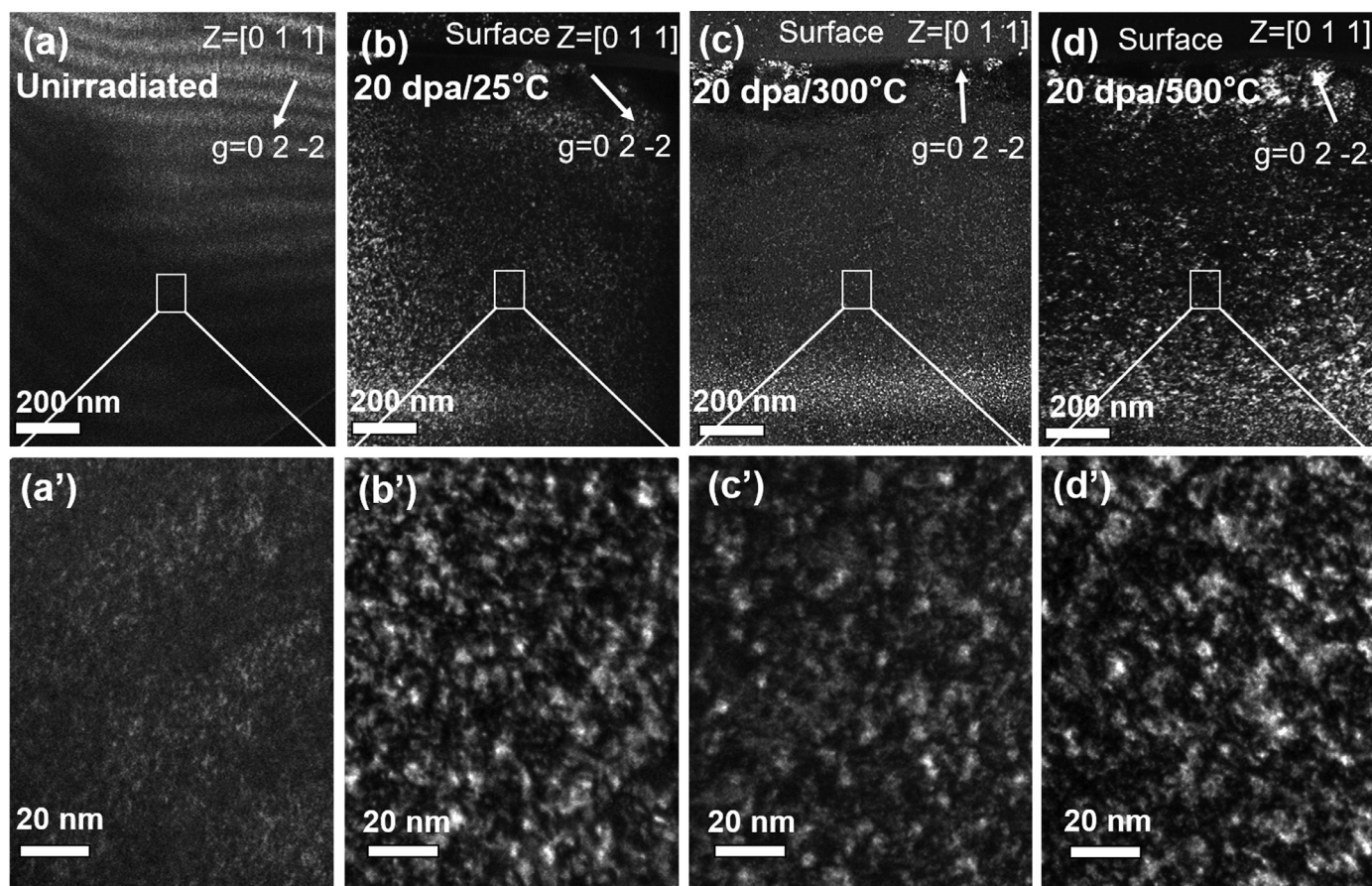
Fig. 4. Weak-beam dark-field TEM images of the cross-sectional microstructures in $(Zr_{0.25}Ta_{0.25}Nb_{0.25}Ti_{0.25})C$ HECC samples (a) before irradiation and after irradiation to 20 dpa at (b) 25, (c) 300, and (d) 500 °C. (a') to (d') are high-magnification images of the rectangle frame area in (a) to (d), respectively. TEM images were taken near the <0 1 1> zone axis to reveal irradiation-induced defect clusters.

Table 1
The set of **g·b** results of a/3<1 1 1> and a/2<1 1 0> type dislocation loops with four different **g** vectors used in Fig. 5.

g\b	Times a/3				Times a/2					
	1 1 1	$\bar{1}$ 1 1	1 $\bar{1}$ 1	1 1 $\bar{1}$	1 1 0	1 $\bar{1}$ 0	1 0 1	$\bar{1}$ 0 1	0 1 1	0 $\bar{1}$ 1
3 $\bar{1}$ 1	**4**	**−3**	**5**	**1**	**2**	**4**	**4**	**−2**	**0**	**2**
2 0 0	2	−2	2	2	2	2	2	−2	0	0
0 2 0	2	2	−2	2	2	−2	0	0	2	−2
2 $\bar{2}$ 0	0	−4	4	0	0	4	2	−2	−2	2

at about 900 nm (Fig. 7b). The trend of the volumetric density of dislocation loops with depth is consistent with the SRIM calculated displacement damage (solid line in Fig. 2, the peak is at 830 nm), but the peak position is slightly deeper. In the SRIM simulation, the target material is assumed to be a solid solution in which the specific crystal structure is not considered [56], so the deviation in the peak damage position may be caused by the rock-salt structure of $(Zr_{0.25}Ta_{0.25}Nb_{0.25}Ti_{0.25})C$. Another possibility is that the high-concentration defect clusters observed at a depth of 900 nm in Fig. 4 may contain Zr^{2+} ion implantations (dashed line in Fig. 2). However, the strain field from the low concentration of ion-implanted Zr (about 0.2 at.%) may not generate significant diffraction contrast in the weak-beam dark-field TEM images, so their contribution is negligible.

These experimental observations show that the dislocation loops remain small in size (several nanometers), even though their density increases significantly with the depth. This indicates that the coalesce and growth of defect clusters may be suppressed by the high-entropy effect in $(Zr_{0.25}Ta_{0.25}Nb_{0.25}Ti_{0.25})C$ at 25–500 °C.

The compositional complexity in $(Zr_{0.25}Ta_{0.25}Nb_{0.25}Ti_{0.25})C$ can induce significant lattice distortion due to the different size and bonding strength of the Zr, Ta, Nb and Ti atoms on the anion positions. Rost et al. used an X-ray absorption fine structure (EXAFS) analysis to conclude that in $Mg_{0.2}Ni_{0.2}Co_{0.2}Cu_{0.2}Zn_{0.2}O$, the distortion from an ideal rock-salt structure occurs primarily through the disorder in the anion FCC sublattice, in which oxygen ions are displaced from the equilibrium locations to accommodate the distortions in the cation polyhedral [57]. Because $(Zr_{0.25}Ta_{0.25}Nb_{0.25}Ti_{0.25})C$ has a similar rock-salt structure with $(Mg_{0.2}Co_{0.2}Ni_{0.2}Cu_{0.2}Zn_{0.2})O$, the lattice distortion in $(Zr_{0.25}Ta_{0.25}Nb_{0.25}Ti_{0.25})C$ may also occur primarily through the anion sublattice. Tong et al. found that local lattice distortion is the dominant factor for the slow growth of dislocation loops in various HEAs with FCC structures after ion irradiations [58]. Thus, the strong local lattice distortion in $(Zr_{0.25}Ta_{0.25}Nb_{0.25}Ti_{0.25})C$ may also suppress the coalesce and growth of defect clusters.

The higher irradiation temperature results in slightly larger diameter (Fig. 7a) and lower volumetric density (Fig. 7b) of dislo-
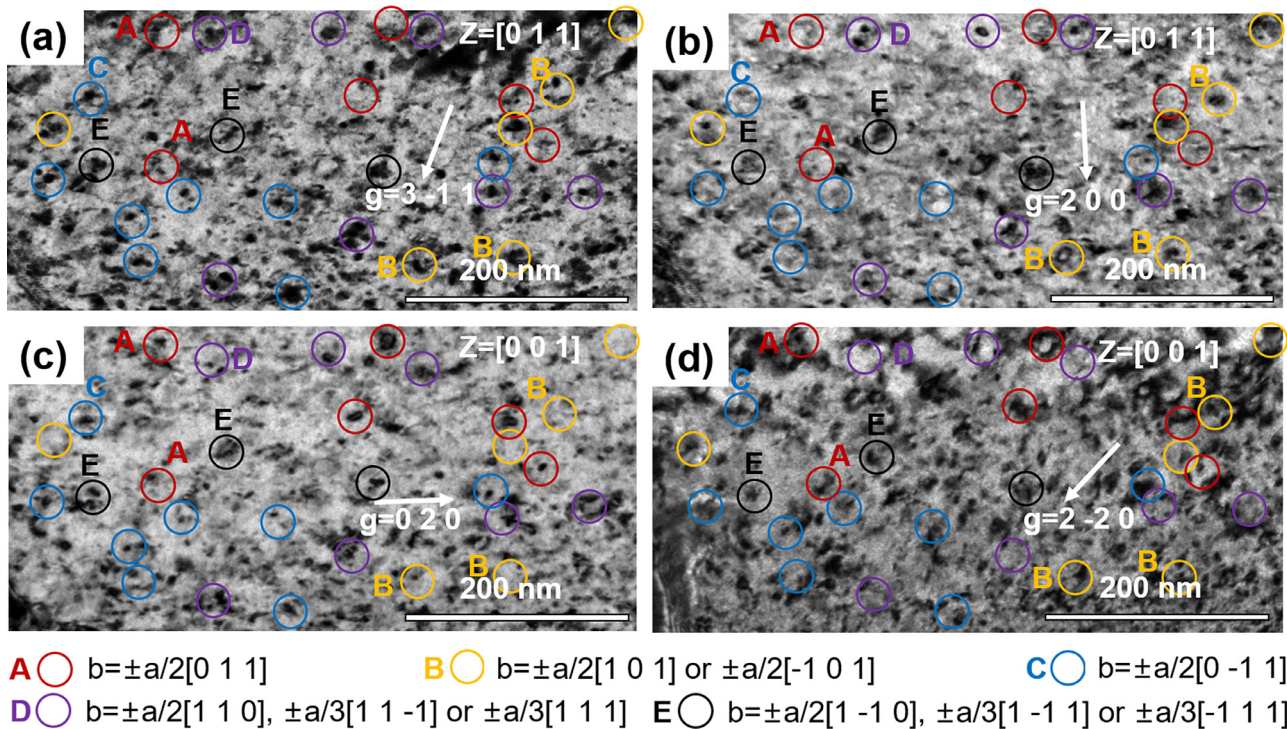
A ⃝ b=±a/2[0 1 1]   B ⃝ b=±a/2[1 0 1] or ±a/2[-1 0 1]   C ⃝ b=±a/2[0 -1 1]
D ⃝ b=±a/2[1 1 0], ±a/3[1 1 -1] or ±a/3[1 1 1]   E ⃝ b=±a/2[1 -1 0], ±a/3[1 -1 1] or ±a/3[-1 1 1]

Fig. 5. Bright-field TEM images of dislocation loops and **g·b** analysis on $(Zr_{0.25}Ta_{0.25}Nb_{0.25}Ti_{0.25})C$ sample after irradiation at 20dpa/500 °C. Dislocation loops with the same Burgers vector are marked by circles in the same color.

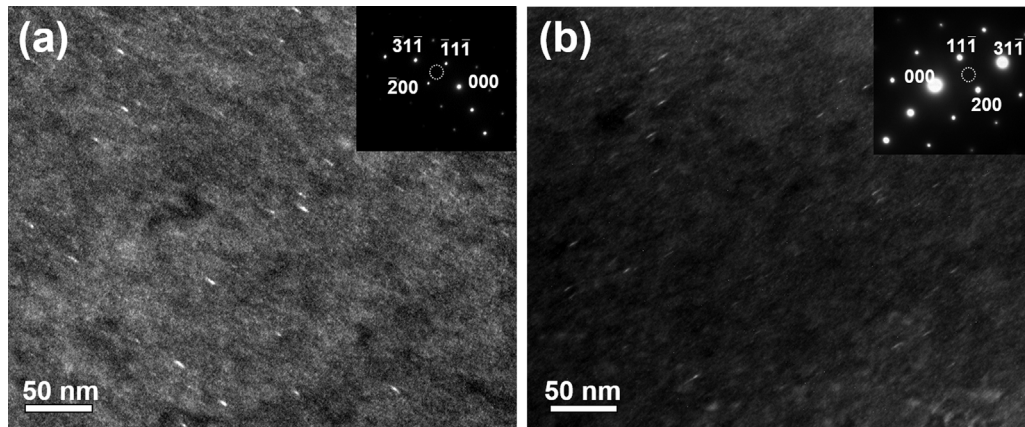Fig. 6. Rel-rod dark-field TEM images of Frank loops in $(Zr_{0.25}Ta_{0.25}Nb_{0.25}Ti_{0.25})C$ sample after irradiation at 20dpa/500 °C under the diffraction conditions of **g**= (a) $(\bar{3}1\bar{1})$ and (b) $(31\bar{1})$ near [0 1 1] zone. (Inset) The corresponding electron diffraction patterns, in which the location of the objective aperture is marked by the dotted circles.

cation loops. This can be explained by the increasing mobility of point defects at high temperatures, leading to the growth of either interstitial- or vacancy-type defect clusters along with the recombination of interstitials and vacancies. The sluggish variation in loop diameter and density as a function of irradiation temperature at 25–500 °C is consistent with literature of other carbide ceramics such as ZrC [38] and Ti_2AlC [59] during heavy ion irradiation, which can be explained as that this temperature range represents relatively low temperatures normalized to their high melting temperature.

There were quantitative characterizations of dislocation loops in other carbide ceramics such as ZrC and TiC. Ulmer et al. [38] investigated the microstructural evolution in $ZrC_{0.9}$ under Kr ion irradiation, which shows that the diameter of dislocation loops has a slight increase with temperature (e.g., 4 nm at 400 °C vs. 5 nm at 600 °C at 3.9 dpa), whereas the volumetric density of dislocation loops reduces slightly with temperature (e.g., 8×10^{22} at 400 °C

vs. 6×10^{22} m^{-3} at 600 °C at 3.9 dpa). Yang et al. [37] reported an average loop diameter of 4.3 and 5.8 nm in ZrC by proton irradiation to 0.7 and 1.5 dpa, respectively, at 800 °C. Snead et al. found that the diameter of dislocation loops is 2 nm at 673 °C while the volumetric density is 2×10^{22} m^{-3} at a neutron fluence of 3.7×10^{25} n/m^2 and 673 °C. Agarwal et al. [52] showed that the diameter of dislocation loops in TiC increased from 5 nm at 620 °C to 20 m at 1115 °C, whereas the volumetric density decreased from 3×10^{22} m^{-3} at 620 °C to 6×10^{21} m^{-3} at 1115 °C after neutron irradiation to 2 dpa. Thus, the observed sluggish variation in loop diameter and number density as a function of irradiation temperature at 25–500 °C in $(Zr_{0.25}Ta_{0.25}Nb_{0.25}Ti_{0.25})C$ is consistent with the literature of ZrC and TiC. However, the direct comparison of dislocation loops between $(Zr_{0.25}Ta_{0.25}Nb_{0.25}Ti_{0.25})C$ and ZrC under the same irradiation conditions will be necessary in the future studies.

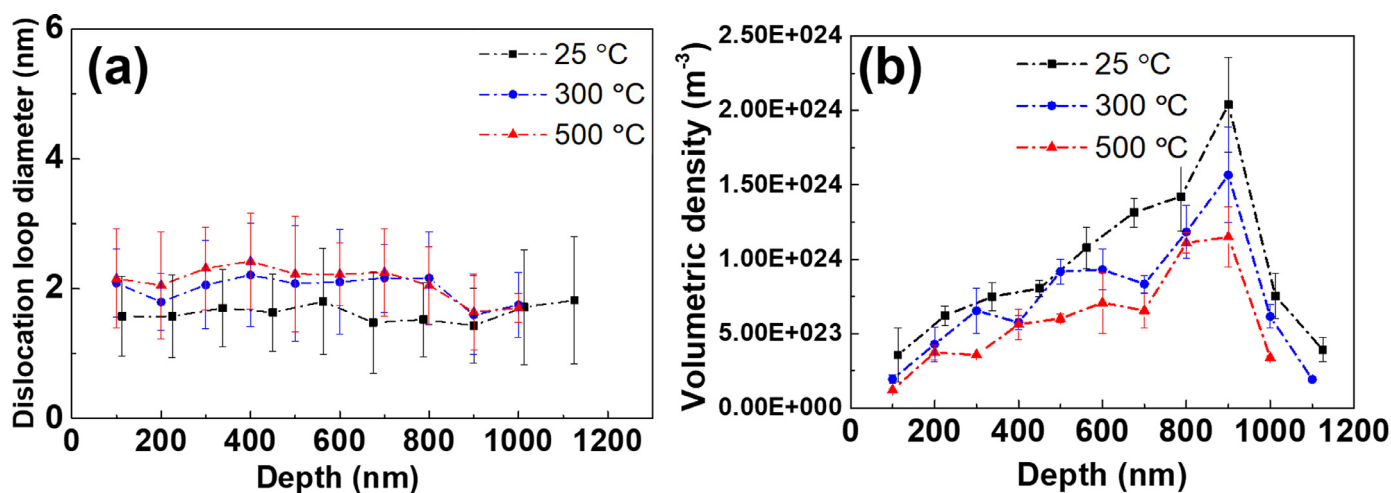**Fig. 7.** (a) The diameter and (b) volumetric density of dislocation loops in $(Zr_{0.25}Ta_{0.25}Nb_{0.25}Ti_{0.25})C$ sample as a function of depth after 3 MeV Zr ion irradiation to 20 dpa at 25, 300, and 500 °C.

Zheng et al. performed *ab initio* calculations of defect migration energies in ZrC, which showed that interstitials have lower migration barriers than vacancies [60]. Due to the high concentration of carbon vacancies in the sub-stoichiometric ZrC_x, carbon interstitials can recombine quickly with these vacancies. Based on these simulation results, Ulmer et al. suggested that Zr interstitials are likely dominant in the nucleation and growth of visible defect clusters in sub-stoichiometric ZrC_x under 1 MeV Kr^{2+} irradiation at −253 to 800 °C . Due to the structural similarity to ZrC, the dislocation loops in observed $(Zr_{0.25}Ta_{0.25}Nb_{0.25}Ti_{0.25})C$ are also likely dominated by the interstitials of metal atoms. Nevertheless, more theoretical and experimental investigations are needed to determine the nature of defect clusters, their nucleation and growth mechanisms, as well as the effect of stoichiometry in $(Zr_{0.25}Ta_{0.25}Nb_{0.25}Ti_{0.25})C$.

3.4. Irradiation-induced voids

Fresnel contrast was used to characterize the potential voids in $(Zr_{0.25}Ta_{0.25}Nb_{0.25}Ti_{0.25})C$ samples after 3 MeV Zr ion irradiation to 20 dpa at 25, 300, and 500 °C, respectively. No detectable voids were found under all these conditions, indicating $(Zr_{0.25}Ta_{0.25}Nb_{0.25}Ti_{0.25})C$ has an excellent void swelling resistance at 25–500 °C.

The void formation in irradiated materials is attributed to the accumulation of vacancies, which usually occurs at elevated temperatures when vacancies have high mobility [61]. The lack of void formation is consistent with the irradiation studies of other carbide ceramics, such as fast neutron irradiation of ZrC by Snead et al. [62] and neutron irradiation of TiC by Agarwal et al. [52]. This was explained by the *ab initio* calculations of defect migration energies in ZrC, which suggested that Zr and C vacancies have high migration barriers [40]. Thus, the void growth in ZrC is suppressed by the low mobility of vacancies. Due to the structural similarity to ZrC, the vacancy migration barrier in $(Zr_{0.25}Ta_{0.25}Nb_{0.25}Ti_{0.25})C$ may be also very high at 25–500 °C, which prevent the void growth. In addition, voids typically form at irradiation temperature of ~0.3–0.6 T_m (T_m=melting temperature). The exact melting temperature of $(Zr_{0.25}Ta_{0.25}Nb_{0.25}Ti_{0.25})C$ was not measured, but is at least above 2000 °C. Thus, 500 °C is below 0.3T_m of $(Zr_{0.25}Ta_{0.25}Nb_{0.25}Ti_{0.25})C$.

3.5. Irradiation-induced segregation

Fig. 8 shows the STEM Z-contrast images of the $(Zr_{0.25}Ta_{0.25}Nb_{0.25}Ti_{0.25})C$ sample after 3 MeV Zr ion irradiation to 20 dpa at 25, 300, and 500 °C, respectively, with the corresponding EDS line scan profiles across the grain boundaries. Random grain boundaries were chosen for the element distribution characterization. Based on the EDS line scan profiles, the Ti, Ta, Nb, and Zr elements have significant local variations that may result from their disorder in the cation position, but exhibiting no obvious element segregation in the grain boundaries. The generally lower Ta concentration was the same in the unirradiated sample, which was possibly caused by the loss of Ta during the ball mill process due to adhesion of Ta to mill balls and jars. In the as-fabricated $(Zr_{0.25}Ta_{0.25}Nb_{0.25}Ti_{0.25})C$ samples, the concentrations of Zr, Ta, Nb, and Ti were measured as 27.5 ± 3%, 18.2 ± 2.2%, 28.6 ± 3.3%, and 25.7 ± 2.8%, respectively according to EDS analysis.

The radiation-induced segregation behavior in materials is often caused by the inverse Kirkendall mechanism, which depends on the coupling between fluxes of point defects and alloying elements [63]. In HECCs, both theoretical and experimental studies are needed to elucidate the effect of compositional complexity on the diffusion of vacancies and interstitials of metal elements. It is noted that the "sluggish diffusion" was a proposed hypothesis in early studies of HEAs, but is not supported by the recent data on the measured diffusion coefficients [64]. For example, Miracle and Senkov suggest that the measured diffusion coefficients in $CoCrFeMn_{0.5}Ni$ are not essentially different from those in metal elements and conventional alloys [64]. Sugita et al., measured the activation energy for vacancy diffusion in a CoCrFeMnNi HEA by the positron lifetime spectroscopy, which is in the same range with the that of self-diffusion in the constituent FCC metals [65]. Thus, the main effect appears as a broadening of the potential migration energies for vacancy motion in HEAs compared to conventional alloys.

It is also noted that the current segregation studies were performed in heavy-ion irradiated materials. Compared with light ions such as neutrons or protons, heavy ion irradiation is more difficult to induce grain boundary segregation due to its high dpa rates [66,67]. For example, Cr deletion and Ni enrichment were less likely observed in heavy-ion irradiated 316 stainless steels [68]. With dramatically increased dpa rates, grain boundary segregation temperatures can be shifted significantly to much higher tempera-
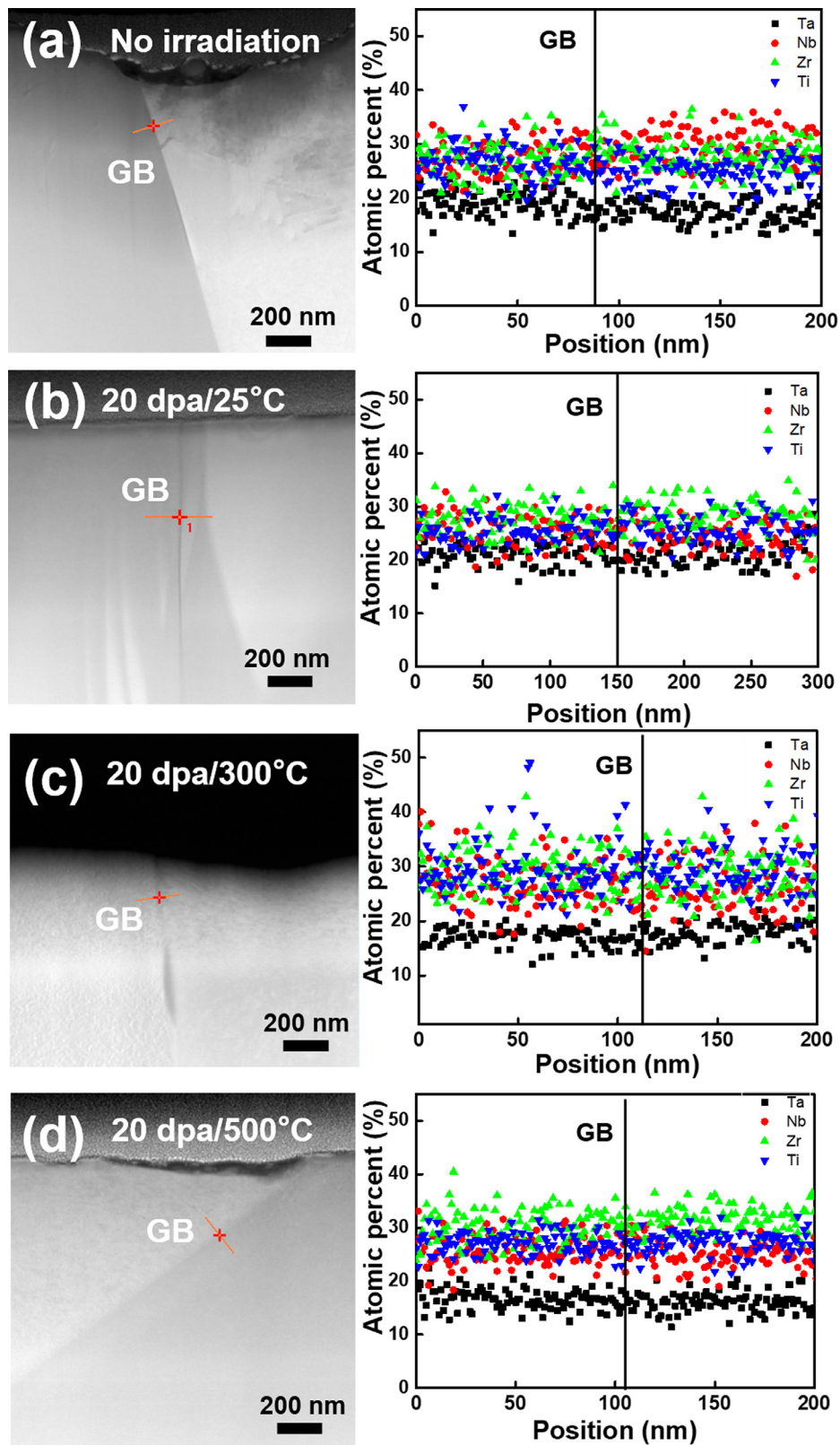
Fig. 8. STEM images with the corresponding EDS line scan profiles of Ti, Ta, Nb, and Zr element distribution across the grain boundaries of $(Zr_{0.25}Ta_{0.25}Nb_{0.25}Ti_{0.25})C$ samples (a) without irradiation and after irradiation to 20 dpa at (b) 25, (c) 300, and (d) 500 °C. GB = grain boundary. The vertical lines in EDS profiles represent the locations of grain boundary.
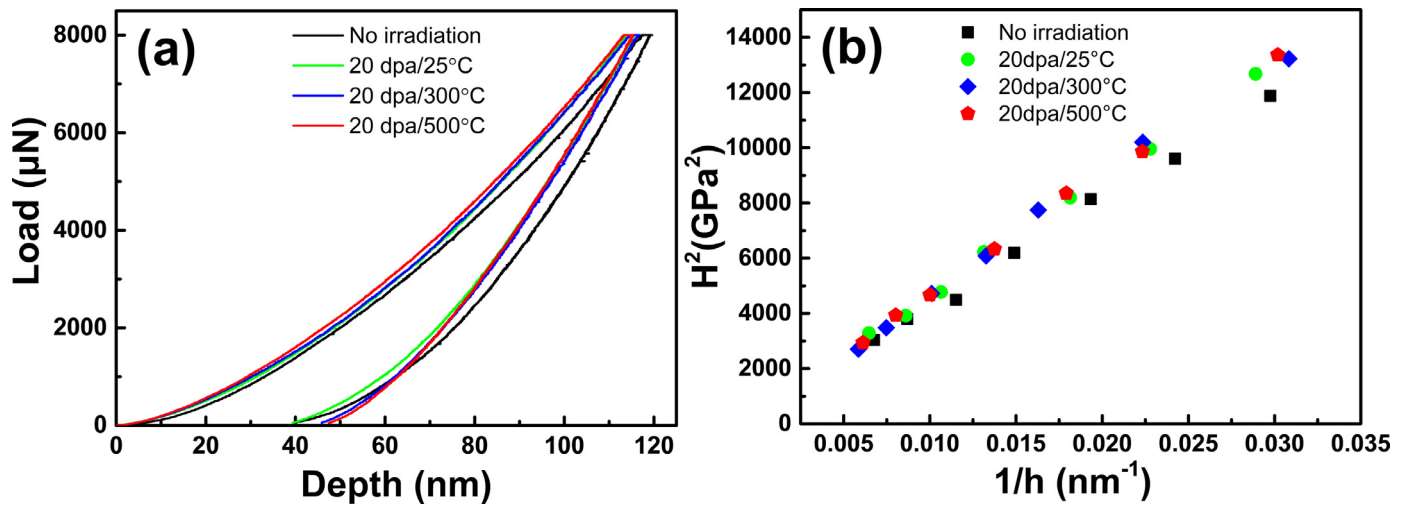
Fig. 9. (a) Nanoindentation load-displacement curves and (b) dependence of H^2 on $1/h$ of $(Zr_{0.25}Ta_{0.25}Nb_{0.25}Ti_{0.25})C$ samples before and after irradiation.

Table 2
Elastic modulus and nanohardness of $(Zr_{0.25}Ta_{0.25}Nb_{0.25}Ti_{0.25})C$ samples before and after irradiation.

	No irradiation	20 dpa/25 °C	20 dpa/300 °C	20 dpa/500 °C
Elastic modulus/GPa	339.5 ± 10.0	353.1 ± 10.0	338.5 ± 12.9	344.3 ± 15.1
Nanohardness/GPa	18.9 ± 1.9	20.8 ± 1.7	20.4 ± 2.1	20.5 ± 1.6

tures [69]. Thus, a full scope of studies on radiation-induced segregation needs to extend to light ion irradiations.

3.6. Nanoindentation test

Because the depth of the irradiation damage is about 1.45 μm (Figs. 2 and 7), nanoindentations were used to evaluate the irradiation-induced changes in mechanical property including hardness and elastic modulus. Nanoindentation test results are sensitive to the microstructure and stress fields about 10 times of the indentation depth [70]. To avoid the influence of the unirradiated material underneath the irradiated layer, the indentation depth should be within 1/10 of the irradiated layer thickness. Fig. 9(a) presents the load-displacement curves of the $(Zr_{0.25}Ta_{0.25}Nb_{0.25}Ti_{0.25})C$ samples before and after 3 MeV Zr ion irradiation at 25, 300, and 500 °C, respectively. Fig. 9(b) plots H^2 vs. $1/h$ for $(Zr_{0.25}Ta_{0.25}Nb_{0.25}Ti_{0.25})C$ samples before and after irradiation, which was used to determine the real hardness (H_0). Table 2 lists the elastic modulus and nanohardness of both the unirradiated and irradiated $(Zr_{0.25}Ta_{0.25}Nb_{0.25}Ti_{0.25})C$ samples. The unirradiated $(Zr_{0.25}Ta_{0.25}Nb_{0.25}Ti_{0.25})C$ exhibited a high nanohardness of 18.9 ± 1.9 GPa, which was consistent with the previous reports on $(Hf_{0.25}Ta_{0.25}Zr_{0.25}Ti_{0.25})C$ and $(Hf_{0.25}Ta_{0.25}Zr_{0.25}Nb_{0.25})C$ [39]. After 20 dpa irradiation at 25 °C, the elastic modulus increased by 4% and the hardness increased by 10% compared to the unirradiated sample. The 4% variation of the elastic modulus is within the measurement errors of the nanoindentation tests. No change in the elastic properties is expected because the composition distribution, density, and phase remain after irradiation. After irradiation at 300 and 500 °C, the elastic modulus was almost the same with the unirradiated sample, while the hardness increase was less significant than that at 25 °C. Similar hardness increase after irradiation was observed in other ceramics such as ZrC, SiC, and MgO [37,71,72]. The irradiation hardening in metals (e.g. stainless steels) is caused by the production of the irradiation-induced obstacles such as dislocation loops and irradiation-induced precipitations, which impede the dislocation motion on the slip plane [73]. Csanádi et al. investigated the slip behavior of $(Hf_{0.25}Ta_{0.25}Zr_{0.25}Nb_{0.25})C$ at room temperature during micro-compression [74]. {110}⟨110⟩ was identified as the primary slip system in micropillar experiments, while {111}⟨110⟩ was assumed as the slip system in the nanoindentation experiments. The slip systems were possibly operated by the activation of partial dislocations. Thus, the observed irradiation-induced hardness increase in $(Hf_{0.25}Ta_{0.25}Zr_{0.25}Nb_{0.25})C$ was possibly caused by irradiation-induced defect clusters (i.e., dislocation loops) that hinder the slip of {111}⟨110⟩ during the nanoindentations. In addition, the lattice strain may also contribute to the increase of hardness after irradiation. Based on the GIXRD results, the lattice expansion was ~0.2% after irradiation, indicating lattice strain in the irradiated layer of the $(Zr_{0.25}Ta_{0.25}Nb_{0.25}Ti_{0.25})C$ samples. Debelle et al. suggest that irradiation leads to build-up of elastic strain in materials due to clustering of interstitial defects into dislocation loops [75]. Chen et al. reported that the hardness of SiC after irradiation depends on the lattice strain [76]. Therefore, the lattice strain from irradiation-induced defects may be another important contributor to the hardness increase in $(Zr_{0.25}Ta_{0.25}Nb_{0.25}Ti_{0.25})C$ samples.

4. Conclusions

(1) $(Zr_{0.25}Ta_{0.25}Nb_{0.25}Ti_{0.25})C$ HECC was synthesized by SPS, which has a single-phase rock-salt structure where Zr, Ta, Nb, and Ti metal elements share the cation sublattice while C is in the anion sublattice.

(2) X-ray diffraction analysis showed that $(Zr_{0.25}Ta_{0.25}Nb_{0.25}Ti_{0.25})C$ maintained high phase stability without phase transformation after 3 MeV Zr ion irradiation to 20 dpa at 25, 300, and 500 °C. However, a lattice parameter expansion of about 0.2% was revealed.

(3) The Burgers vectors, diameter, number density, and distribution of irradiation-induced defect clusters were characterized by TEM. The irradiation-induced microstructures are comprised of defect clusters with a diameter of several nanometers, which are characterized as perfect loops with Burgers vectors of $\boldsymbol{b} = a/2\langle 1\,1\,0\rangle$ and faulted Frank loops with Burgers vectors of $\boldsymbol{b} = a/3\langle 1\,1\,1\rangle$. The growth of dislocation loops may be suppressed by the strong local lattice distortion caused by the compositional complexity.

(4) No void formation was observed, which may be caused by high vacancy migration barriers in carbide ceramics.

(5) No radiation-induced segregation near grain boundaries was detected.

(6) Nanoindentation tests showed irradiation-induced hardness increase, which was possibly caused by dislocation loops as barriers to impede the slip during nanoindentations, as well as the lattice strain.

(7) The combination of high irradiation resistance with other physical properties such as high melting temperature and hardness indicates HECCs are promising structural materials for Generation-IV nuclear systems such as GFR and VHTR.

Declaration of Competing Interest

The authors declare that they have no known competing financial interests or personal relationships that could have appeared to influence the work reported in this paper.

Acknowledgments

References

[1] S.J. Zinkle, G.S. Was, Materials challenges in nuclear energy, Acta Mater. 61 (2013) 735–758.

[2] P. Hosemann, D. Frazer, M. Fratoni, A. Bolind, M.F. Ashby, Materials selection for nuclear applications: challenges and opportunities, Scr. Mater. 143 (2018) 181–187.

[3] Y. Zhang, T.T. Zuo, Z. Tang, M.C. Gao, K.A. Dahmen, P.K. Liaw, Z.P. Lu, Microstructures and properties of high-entropy alloys, Prog. Mater. Sci. 61 (2014) 1–93.

[4] X. Yan, X. Zhang, F. Wang, T. Stockdale, Y. Dzenis, M. Nastasi, B. Cui, Fabrication of ODS Austenitic Steels and CoCrFeNi high-entropy alloys by spark plasma sintering for nuclear energy applications, JOM 71 (2019) 2856–2867.

[5] M.-H. Tsai, J.-W. Yeh, High-entropy alloys: a critical review, Mater. Res. Lett. 2 (2014) 107–123.

[6] K.-Y. Tsai, M.-H. Tsai, J.-W. Yeh, Sluggish diffusion in Co-Cr-Fe-Mn-Ni high-entropy alloys, Acta Mater. 61 (2013) 4887–4897.

[7] B. Schuh, F. Mendez-Martin, B. Völker, E.P. George, H. Clemens, R. Pippan, A. Hohenwarter, Mechanical properties, microstructure and thermal stability of a nanocrystalline CoCrFeMnNi high-entropy alloy after severe plastic deformation, Acta Mater. 96 (2015) 258–268.

[8] Y. Lu, Y. Dong, S. Guo, L. Jiang, H. Kang, T. Wang, B. Wen, Z. Wang, J. Jie, Z. Cao, A promising new class of high-temperature alloys: eutectic high-entropy alloys, Sci. Rep. 4 (2014) 6200.

[9] X.-W. Qiu, Y.-P. Zhang, L. He, C. Liu, Microstructure and corrosion resistance of AlCrFeCuCo high entropy alloy, J. Alloy. Compd. 549 (2013) 195–199.

[10] Y.-J. Hsu, W.-C. Chiang, J.-K. Wu, Corrosion behavior of FeCoNiCrCux high-entropy alloys in 3.5% sodium chloride solution, Mater. Chem. Phys. 92 (2005) 112–117.

[11] A. Kareer, J.C. Waite, B. Li, A. Couet, D.E.J. Armstrong, A.J. Wilkinson, Low activation, refractory, high entropy alloys for nuclear applications, J. Nucl. Mater. 526 (2019) 151744.

[12] O. El-Atwani, N. Li, M. Li, A. Devaraj, J.K.S. Baldwin, M.M. Schneider, D. Sobieraj, J.S. Wróbel, D. Nguyen-Manh, S.A. Maloy, Outstanding radiation resistance of tungsten-based high-entropy alloys, Sci. Adv. 5 (2019) eaav2002.

[13] N.K. Kumar, C. Li, K.J. Leonard, H. Bei, S.J. Zinkle, Microstructural stability and mechanical behavior of FeNiMnCr high entropy alloy under ion irradiation, Acta Mater. 113 (2016) 230–244.

[14] Y. Lu, H. Huang, X. Gao, C. Ren, J. Gao, H. Zhang, S. Zheng, Q. Jin, Y. Zhao, C. Lu, A promising new class of irradiation tolerant materials: Ti2ZrHfV0. 5Mo0. 2 high-entropy alloy, J. Mater. Sci. Technol. 35 (2019) 369–373.

[15] T. Egami, W. Guo, P.D. Rack, T. Nagase, Irradiation resistance of multicomponent alloys, Metall. Mater. Trans. A 45 (2014) 180–183.

[16] Y. Zhang, G.M. Stocks, K. Jin, C. Lu, H. Bei, B.C. Sales, L. Wang, L.K. Béland, R.E. Stoller, G.D. Samolyuk, Influence of chemical disorder on energy dissipation and defect evolution in concentrated solid solution alloys, Nat. Commun. 6 (2015) 8736.

[17] D. Bérardan, S. Franger, D. Dragoe, A.K. Meena, N. Dragoe, Colossal dielectric constant in high entropy oxides, Phys. Status Solidi RRL–Rapid Res. Lett. 10 (2016) 328–333.

[18] D. Bérardan, S. Franger, A.K. Meena, N. Dragoe, Room temperature lithium superionic conductivity in high entropy oxides, J. Mater. Chem. A 4 (2016) 9536–9541.

[19] J. Gild, Y. Zhang, T. Harrington, S. Jiang, T. Hu, M.C. Quinn, W.M. Mellor, N. Zhou, K. Vecchio, J. Luo, High-entropy metal diborides: a new class of high-entropy materials and a new type of ultrahigh temperature ceramics, Sci. Rep. 6 (2016) 37946.

[20] Y. Zhang, W.-M. Guo, Z.-B. Jiang, Q.-Q. Zhu, S.-K. Sun, Y. You, K. Plucknett, H.-T. Lin, Dense high-entropy boride ceramics with ultra-high hardness, Scr. Mater. 164 (2019) 135–139.

[21] J. Zhou, J. Zhang, F. Zhang, B. Niu, L. Lei, W. Wang, High-entropy carbide: a novel class of multicomponent ceramics, Ceram. Int. 44 (2018) 22014–22018.

[22] X. Yan, L. Constantin, Y. Lu, J.-F. Silvain, M. Nastasi, B. Cui, (Hf0. 2Zr0. 2Ta0. 2Nb0. 2Ti0. 2) C high-entropy ceramics with low thermal conductivity, J. Am. Ceram. Soc. 101 (2018) 4486–4491.

[23] P. Sarker, T. Harrington, C. Toher, C. Oses, M. Samiee, J.-P. Maria, D.W. Brenner, K.S. Vecchio, S. Curtarolo, High-entropy high-hardness metal carbides discovered by entropy descriptors, Nat. Commun. 9 (2018) 1–10.

[24] D. Demirskyi, H. Borodianska, T.S. Suzuki, Y. Sakka, K. Yoshimi, O. Vasylkiv, High-temperature flexural strength performance of ternary high-entropy carbide consolidated via spark plasma sintering of TaC, ZrC and NbC, Scr. Mater. 164 (2019) 12–16.

[25] Y. Yang, W. Wang, G.-Y. Gan, X.-F. Shi, B.-Y. Tang, Structural, mechanical and electronic properties of (TaNbHfTiZr) C high entropy carbide under pressure: ab initio investigation, Phys. B Condens. Matter. 550 (2018) 163–170.

[26] B. Ye, T. Wen, D. Liu, Y. Chu, Oxidation behavior of (Hf0. 2Zr0. 2Ta0. 2Nb0. 2Ti0. 2) C high-entropy ceramics at 1073–1473K in air, Corros. Sci. 153 (2019) 327–332.

[27] B. Ye, T. Wen, Y. Chu, High-temperature oxidation behavior of (Hf0. 2Zr0. 2Ta0. 2Nb0. 2Ti0. 2) C high-entropy ceramics in air, J. Am. Ceram. Soc. 103 (2020) 500–507.

[28] Y. Tan, C. Chen, S. Li, X. Han, J. Xue, T. Liu, X. Zhou, H. Zhang, Oxidation behaviours of high-entropy transition metal carbides in 1200°C water vapor, J. Alloy. Compd. 816 (2020) 152523.

[29] F. Wang, X. Yan, L. Shao, M. Nastasi, B. Cui, Irradiation damage behavior in novel high-entropy carbide ceramics, Transactions 120 (2019) 327.

[30] Y. Zhang, K. Jin, H. Xue, C. Lu, R.J. Olsen, L.K. Beland, M.W. Ullah, S. Zhao, H. Bei, D.S. Aidhy, Influence of chemical disorder on energy dissipation and defect evolution in advanced alloys, J. Mater. Res. 31 (2016) 2363–2375.

[31] F. Granberg, K. Nordlund, M.W. Ullah, K. Jin, C. Lu, H. Bei, L.M. Wang, F. Djurabekova, W.J. Weber, Y. Zhang, Mechanism of radiation damage reduction in equiatomic multicomponent single phase alloys, Phys. Rev. Lett. 116 (2016) 135504.

[32] C. Lu, L. Niu, N. Chen, K. Jin, T. Yang, P. Xiu, Y. Zhang, F. Gao, H. Bei, S. Shi, Enhancing radiation tolerance by controlling defect mobility and migration pathways in multicomponent single-phase alloys, Nat. Commun. 7 (2016) 1–8.

[33] M.-R. He, S. Wang, S. Shi, K. Jin, H. Bei, K. Yasuda, S. Matsumura, K. Higashida, I.M. Robertson, Mechanisms of radiation-induced segregation in CrFeCoNi-based single-phase concentrated solid solution alloys, Acta Mater. 126 (2017) 182–193 https://doi.org/10.1016/j.actamat.2016.12.046.

[34] D. Gosset, M. Dollé, D. Simeone, G. Baldinozzi, L. Thomé, Structural evolution of zirconium carbide under ion irradiation, J. Nucl. Mater. 373 (2008) 123–129 https://doi.org/10.1016/j.jnucmat.2007.05.034.

[35] K.D. Weaver, T.C. Totemeier, D.E. Clark, Gen IV nuclear energy systems, gas-cooled fast reactor (GFR). FY-04 annual report, Ida. Natl. Eng. Environ. Lab. Ida. Falls Ida. USA. (2004).

[36] K. Sawa, S. Ueta, Research and development on HTGR fuel in the HTTR project, Nucl. Eng. Des. 233 (2004) 163–172.

[37] Y. Yang, C.A. Dickerson, H. Swoboda, B. Miller, T.R. Allen, Microstructure and mechanical properties of proton irradiated zirconium carbide, J. Nucl. Mater. 378 (2008) 341–348 https://doi.org/10.1016/j.jnucmat.2008.06.042.

[38] C.J. Ulmer, A.T. Motta, M.A. Kirk, In situ ion irradiation of zirconium carbide, J. Nucl. Mater. 466 (2015) 606–614.

[39] E. Castle, T. Csanádi, S. Grasso, J. Dusza, M. Reece, Processing and properties of high-entropy ultra-high temperature carbides, Sci. Rep. 8 (2018) 1–12.

[40] R.E. Stoller, M.B. Toloczko, G.S. Was, A.G. Certain, S. Dwaraknath, F.A. Garner,

On the use of SRIM for computing radiation damage exposure, Nucl. Instrum. Methods Phys. Res. Sect. B Beam Interact. Mater. At. 310 (2013) 75–80.

[41] W.J. Weber, Y. Zhang, Predicting damage production in monoatomic and multi-elemental targets using stopping and range of ions in matter code: challenges and recommendations, Curr. Opin. Solid State Mater. Sci. 23 (2019) 100757 https://doi.org/10.1016/j.cossms.2019.06.001.

[42] C. Frontera, J. Rodríguez-Carvajal, FullProf as a new tool for flipping ratio analysis, Phys. B Condens. Matter. 335 (2003) 219–222 https://doi.org/10.1016/S0921-4526(03)00241-2.

[43] M.L. Jenkins, Characterisation of radiation-damage microstructures by TEM, J. Nucl. Mater. 216 (1994) 124–156 https://doi.org/10.1016/0022-3115(94)90010-8.

[44] S.J. Bull, T.F. Page, E.H. Yoffe, An explanation of the indentation size effect in ceramics, Philos. Mag. Lett. 59 (1989) 281–288.

[45] W.D. Nix, H. Gao, Indentation size effects in crystalline materials: a law for strain gradient plasticity, J. Mech. Phys. Solids 46 (1998) 411–425 https://doi.org/10.1016/S0022-5096(97)00086-0.

[46] R. Florez, M.L. Crespillo, X. He, T.A. White, G. Hilmas, W. Fahrenholtz, J. Graham, The irradiation response of ZrC ceramics under 10 MeV Au^{3+} ion irradiation at 800 °C, J. Eur. Ceram. Soc. 40 (2020) 1791–1800 https://doi.org/10.1016/j.jeurceramsoc.2020.01.025.

[47] P. Patriarca, W.O. Harms, Fuels and Materials Development Program, Oak Ridge National Lab TN, 1969.

[48] G.W. Keilholtz, R.E. Moore, M.F. Osborne, Fast-neutron effects on the carbides of titanium, zirconium, tantalum, niobium, and tungsten, Nucl. Appl. 4 (1968) 330–336.

[49] S. Pellegrino, J.-P. Crocombette, A. Debelle, T. Jourdan, P. Trocellier, L. Thomé, Multi-scale simulation of the experimental response of ion-irradiated zirconium carbide: role of interstitial clustering, Acta Mater. 102 (2016) 79–87 https://doi.org/10.1016/j.actamat.2015.09.004.

[50] J. Gan, M.K. Meyer, R.C. Birtcher, T.R. Allen, Microstructure evolution in ZrC irradiated with Kr ions, (n.d.) 7.

[51] Y. Yang, C.A. Dickerson, H. Swoboda, B. Miller, T.R. Allen, Microstructure and mechanical properties of proton irradiated zirconium carbide, J. Nucl. Mater. 378 (2008) 341–348 https://doi.org/10.1016/j.jnucmat.2008.06.042.

[52] S. Agarwal, T. Koyanagi, A. Bhattacharya, L. Wang, Y. Katoh, X. Hu, M. Pagan, S.J. Zinkle, Neutron irradiation-induced microstructure damage in ultra-high temperature ceramic TiC, Acta Mater. 186 (2020) 1–10.

[53] E.H. Lee, T.S. Byun, J.D. Hunn, K. Farrell, L.K. Mansur, Origin of hardening and deformation mechanisms in irradiated 316 LN austenitic stainless steel, J. Nucl. Mater. 296 (2001) 183–191.

[54] C. Sun, M. Song, K.Y. Yu, Y. Chen, M. Kirk, M. Li, H. Wang, X. Zhang, In situ evidence of defect cluster absorption by grain boundaries in Kr ion irradiated nanocrystalline Ni, Metall. Mater. Trans. A 44 (2013) 1966–1974.

[55] B.H. Sencer, G.M. Bond, F.A. Garner, M.L. Hamilton, B.M. Oliver, L.E. Thomas, S.A. Maloy, W.F. Sommer, M.R. James, P.D. Ferguson, Microstructural evolution of Alloy 718 at high helium and hydrogen generation rates during irradiation with 600–800 MeV protons, J. Nucl. Mater. 283 (2000) 324–328.

[56] D.P. Hickey, Ion Implantation Induced Defect Formation and Amorphization in the Group IV Semiconductors: Diamond, Silicon, and Germanium, University of Florida, 2007.

[57] C.M. Rost, Z. Rak, D.W. Brenner, J.-P. Maria, Local structure of the MgxNixCox-CuxZnxO (x= 0.2) entropy-stabilized oxide: an EXAFS study, J. Am. Ceram. Soc. 100 (2017) 2732–2738.

[58] Y. Tong, G. Velisa, S. Zhao, W. Guo, T. Yang, K. Jin, C. Lu, H. Bei, J.Y.P. Ko, D.C. Pagan, Evolution of local lattice distortion under irradiation in medium-and high--entropy alloys, Materialia 2 (2018) 73–81.

[59] F. Wang, Q. Su, M. Nastasi, M.A. Kirk, M. Li, B. Cui, Evolution of irradiation defects in Ti2AlC ceramics during heavy ion irradiation, Ceram. Int. 44 (2018) 14686–14692.

[60] M.-J. Zheng, I. Szlufarska, D. Morgan, Defect kinetics and resistance to amorphization in zirconium carbide, J. Nucl. Mater. 457 (2015) 343–351.

[61] B.N. Singh, S.J. Zinkle, Defect accumulation in pure FCC metals in the transient regime: a review, J. Nucl. Mater. 206 (1993) 212–229.

[62] L.L. Snead, Y. Katoh, S. Kondo, Effects of fast neutron irradiation on zirconium carbide, J. Nucl. Mater. 399 (2010) 200–207 https://doi.org/10.1016/j.jnucmat.2010.01.020.

[63] T.R. Anthony, Solute segregation in vacancy gradients generated by sintering and temperature changes, Acta Metall. 17 (1969) 603–609.

[64] D.B. Miracle, O.N. Senkov, A critical review of high entropy alloys and related concepts, Acta Mater. 122 (2017) 448–511 https://doi.org/10.1016/j.actamat.2016.08.081.

[65] K. Sugita, N. Matsuoka, M. Mizuno, H. Araki, Vacancy formation enthalpy in CoCrFeMnNi high-entropy alloy, Scr. Mater. 176 (2020) 32–35 https://doi.org/10.1016/j.scriptamat.2019.09.033.

[66] S.M. Bruemmer, E.P. Simonen, P.M. Scott, P.L. Andresen, G.S. Was, J.L. Nelson, Radiation-induced material changes and susceptibility to intergranular failure of light-water-reactor core internals, J. Nucl. Mater. 274 (1999) 299–314.

[67] G.S. Was, T. Allen, Radiation-induced segregation in multicomponent alloys: effect of particle type, Mater. Charact. 32 (1994) 239–255.

[68] T.R. Allen, J.I. Cole, C.L. Trybus, D.L. Porter, H. Tsai, F. Garner, E.A. Kenik, T. Yoshitake, J. Ohta, The effect of dose rate on the response of austenitic stainless steels to neutron radiation, J. Nucl. Mater. 348 (2006) 148–164 https://doi.org/10.1016/j.jnucmat.2005.09.011.

[69] A. Etienne, B. Radiguet, N.J. Cunningham, G.R. Odette, P. Pareige, Atomic scale investigation of radiation-induced segregation in austenitic stainless steels, J. Nucl. Mater. 406 (2010) 244–250 https://doi.org/10.1016/j.jnucmat.2010.08.043.

[70] C. ASTM, 1327-03, Stand. Test method vickers indentation hardness adv. ceram. (2003).

[71] T. Iseki, M. Tezuka, C.-S. Kim, T. Suzuki, H. Suematsu, T. Yano, Hardening by point defects in neutron irradiated A1N and SiC, J. Nucl. Sci. Technol. 30 (1993) 68–77 https://doi.org/10.1080/18811248.1993.9734450.

[72] H. Suematsu, T. Iseki, T. Yano, Y. Saito, T. Suzuki, T. Mori, Point defect hardening in MgO3Al2O3, J. Am. Ceram. Soc. 75 (1992) 1742–1747 https://doi.org/10.1111/j.1151-2916.1992.tb07191.x.

[73] G.S. WAS, Fundamentals of Radiation Materials Science: Metals and Alloys, Springer, 2016.

[74] T. Csanádi, E. Castle, M.J. Reece, J. Dusza, Strength enhancement and slip behaviour of high-entropy carbide grains during micro-compression, Sci. Rep. 9 (2019) 10200 https://doi.org/10.1038/s41598-019-46614-w.

[75] A. Debelle, J.-P. Crocombette, A. Boulle, A. Chartier, T. Jourdan, S. Pellegrino, D. Bachiller-Perea, D. Carpentier, J. Channagiri, T.-H. Nguyen, F. Garrido, L. Thomé, Lattice strain in irradiated materials unveils a prevalent defect evolution mechanism, Phys. Rev. Mater. 2 (2018) 013604 https://doi.org/10.1103/PhysRevMaterials.2.013604.

[76] X. Chen, W. Zhou, Q. Feng, J. Zheng, X. Liu, B. Tang, J. Li, J. Xue, S. Peng, Irradiation effects in 6H–SiC induced by neutron and heavy ions: Raman spectroscopy and high-resolution XRD analysis, J. Nucl. Mater. 478 (2016) 215–221 https://doi.org/10.1016/j.jnucmat.2016.06.020.